catalysts

MDPI

Article

Exceptional Photocatalytic Performance of the $LaFeO_3$/g-C_3N_4 Z-Scheme Heterojunction for Water Splitting and Organic Dyes Degradation

Muhammad Humayun [1,*], Ayesha Bahadur [2], Abbas Khan [1,3] and Mohamed Bououdina [1,*]

[1] Department of Mathematics and Sciences, College of Humanities and Sciences, Energy, Water, and Environment Lab, Prince Sultan University, Riyadh 11586, Saudi Arabia; abbas053@gmail.com
[2] Department of Chemistry, Bacha Khan University Charsadda, Charsadda 24420, Pakistan; aliali95141@gmail.com
[3] Department of Chemistry, Abdul Wali Khan University Mardan, Mardan 23200, Pakistan
* Correspondence: mhumayun@psu.edu.sa (M.H.); mbououdina@psu.edu.sa (M.B.)

Abstract: To simulate natural photosynthesis, scientists have developed an artificial Z-scheme system that splits water into hydrogen and oxygen using two different semiconductors. Researchers are striving to improve the performance of Z-scheme systems by improving light absorption, developing redox couples with high stability, and finding new cocatalysts. Here, we report the synthesis and utilization of $LaFeO_3$/g-C_3N_4 as a Z-scheme system for water reduction to produce hydrogen and organic dye degradation under visible light irradiation. The as-fabricated photocatalyst revealed exceptional activity for H_2 production (i.e., 351 μmol $h^{-1}g^{-1}$), which is 14.6 times higher compared to that of the single-component g-C_3N_4 (i.e., 24 μmol $h^{-1}g^{-1}$). In addition, the composite photocatalyst degraded 87% of Methylene Blue (MB) and 94% of Rhodamine B (RhB) in 2 h. Various experimental analyses confirmed that the exceptional performance of the $LaFeO_3$/g-C_3N_4 Z-scheme catalyst is due to remarkably enhanced charge carrier separation and improved light absorption. The development of this highly effective Z-scheme heterostructure photocatalyst will pave the way for the sustainable development of newly designed Z-scheme scheme systems that will tackle energy and environmental crises.

Keywords: photocatalysis; hydrogen evolution; visible light; organic dyes; Z-scheme

Citation: Humayun, M.; Bahadur, A.; Khan, A.; Bououdina, M. Exceptional Photocatalytic Performance of the $LaFeO_3$/g-C_3N_4 Z-Scheme Heterojunction for Water Splitting and Organic Dyes Degradation. *Catalysts* **2023**, *13*, 907. https://doi.org/10.3390/catal13050907

Academic Editors: Yongming Fu and Qian Zhang

Received: 23 March 2023
Revised: 14 May 2023
Accepted: 18 May 2023
Published: 20 May 2023

1. Introduction

Energy and environmental issues are intricately linked and have emerged as two of the world's most important concerns [1]. The ongoing use of fossil fuels for energy generation has caused substantial environmental damage, such as climate change, air pollution, and water contamination [2,3]. In consequence, there has been an increasing trend toward adopting cleaner renewable energy sources such as wind, solar, and hydropower to alleviate the impact of these challenges [4]. Energy efficiency and conservation techniques are also being adopted in order to reduce energy usage and greenhouse gas emissions [5]. The transition to a more sustainable energy system is critical to ensure a healthier and more sustainable environment for future generations [6–8].

Recently, heterostructure semiconductor photocatalytic technology has gained increasing interest due to its potential to directly utilize solar energy and transform it into chemical energy, which can then be employed in a variety of applications such as the generation of solar fuels such as hydrogen and hydrocarbon fuels, air cleaning, as well as the degradation of various contaminants [9–14]. The method employs semiconductors, which absorb light energy and generate electron–hole pairs, which subsequently react with other molecules to form new compounds [15–17]. Photocatalytic processes take place on the semiconductors'

surfaces, which serve as catalysts. One of the major advantages of semiconductor photocatalysis is its ability to perform under ambient conditions without the need for additional energy sources. As a result, it is a potential technology for long-term and cost-effective environmental remediation and energy generation. However, increasing the process's efficiency and selectivity remains a difficulty, and further research is needed to increase the practicality and scalability of semiconductor photocatalysis [18–21].

Recently, the 2D layered material g-C_3N_4 received promising attention in photocatalysis due to its unique features compared to the other semiconductors. g-C_3N_4 is composed of C and N atoms that are stacked together. Since g-C_3N_4 possesses a narrow bandgap (i.e., 2.7 eV), making it an effective catalyst for visible-light-driven reactions. It has exceptional chemical stability, biocompatibility, and an environmentally friendly nature. Various photocatalytic reactions including CO_2 reduction, organic pollutant degradation, and hydrogen production have all been performed by g-C_3N_4 photocatalysts. Nevertheless, enhancing the photocatalytic activities and understanding the fundamental mechanism of g-C_3N_4 photocatalysis still remain challenging [22–24].

Several strategies including structural modification, heterojunction formation, and co-catalyst loading have been developed with the aim to optimize the catalytic activities of g-C_3N_4. Among these, the heterojunction formation involves the coupling of other semiconductors with g-C_3N_4, to enhance charge separation and transfer. This strategy has shown significant improvements in the catalytic performance of g-C_3N_4 for a wide range of purposes [25]. Among various sorts of heterojunctions, g-C_3N_4-based Z-scheme systems have a great potential for energy and environmental applications due to their high efficiency and flexibility.

The $LaFeO_3$ photocatalyst, on the other hand, is a promising semiconductor photocatalytic utilized for various applications owing to its exceptional electronic and structural features. It is a perovskite-type oxide composed of lanthanum, iron, and oxygen atoms organized in a crystalline lattice. $LaFeO_3$ exhibits a narrow bandgap (i.e., 1.8–2.1 eV), which renders it a highly effective photocatalyst for catalytic reactions triggered by visible light. It also possesses excellent chemical and thermal stability, as well as outstanding biocompatibility. However, due to its inadequate conduction band potential for the water reduction reaction, the practical application of the $LaFeO_3$ photocatalyst remains challenging. However, it has excellent performance for pollutant degradation [26].

Thus, the coupling of $LaFeO_3$ with g-C_3N_4 is highly crucial to improve its catalytic performance. When the two materials are coupled, the absorbed light can be efficiently utilized over a wider spectral range, resulting in enhanced photocatalytic performance. Additionally, the $LaFeO_3$/g-C_3N_4 heterojunction can facilitate charge carrier separation and transfer, thereby enhancing photocatalytic efficiency. It has been shown that the coupling of $LaFeO_3$ with g-C_3N_4 remarkably improves its catalytic activity for various applications [27–29].

Herein, we report the synthesis of $LaFeO_3$/g-C_3N_4 as a Z-scheme heterostructure photocatalyst for H_2 production and degradation of organic dyes. The heterostructure photocatalyst revealed enhanced performance by producing 351 μmol $h^{-1}g^{-1}$ of H_2 through water splitting and degraded 87 and 94% of MB and RhB dyes, respectively. The superior activities of the $LaFeO_3$/g-C_3N_4 catalyst are accredited to the promoted charge transfer and separation and the extended light absorption. This work provides a promising route for the design and implementation of efficient and sustainable catalysts for environmental remediation and energy production.

2. Results and Discussion

2.1. Structural Characterization and Chemical Composition

The XRD patterns of the synthesized photocatalysts are displayed in Figure 1a. The (100) and (002) crystal planes in g-C_3N_4 are represented by diffraction peaks at 12.9° and 27.7°, respectively (JCPDS No. 87-1526). In-plane trigonal nitrogen-linked tri-s-triazine connected-layer units correlate to the weaker peak at the 2-theta value of 12.9°. The stronger

peak at a 2-theta value of 27.4° is associated with the stacking of heptazine rings, which has a 0.32 nm interlayer-distance (inter-planar stacking of conjugated aromatic segments) [30,31]. Diffraction peaks at 22.6°, 32.2°, 39.6°, 46.1°, 57.4°, and 67.3° in $LaFeO_3$ photocatalyst are indexed to the orthorhombic phase and reflect the (002), (112), (022), (004), (204), and (040) crystal planes, respectively (JCPDS No. 37-1493) [32,33]. The distinctive peak of $LaFeO_3$ in the $LaFeO_3/g\text{-}C_3N_4$ catalyst corresponds to the (202) plane, which indicates that the $LaFeO_3$ and $g\text{-}C_3N_4$ surfaces coexist without any observable impurities, indicating that the nanocomposite was successfully formed.

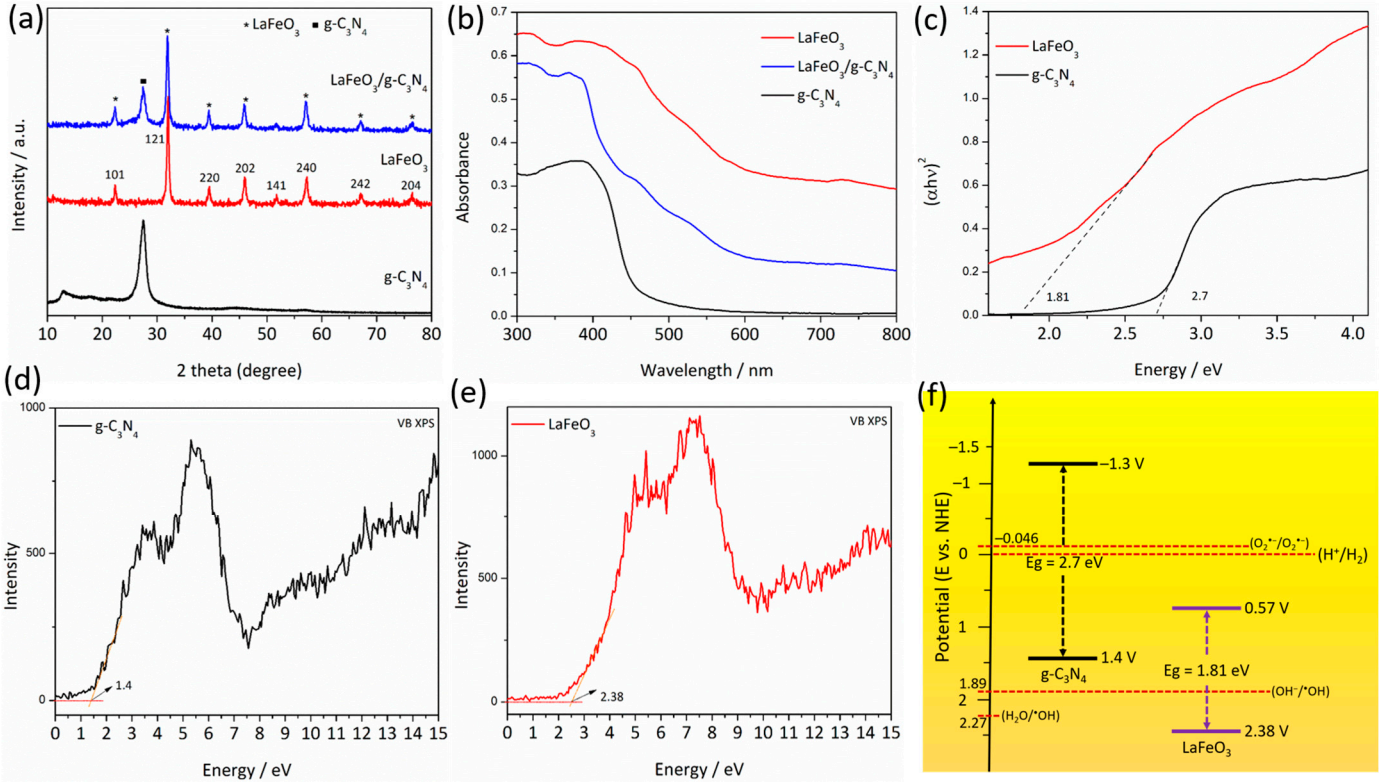

Figure 1. (**a**) XRD patterns and (**b**) UV-visible absorption spectra of $g\text{-}C_3N_4$, $LaFeO_3$, and $LaFeO_3/g\text{-}C_3N_4$ photocatalysts. (**c**) Estimated energy band gaps, (**d**,**e**) valence band XPS spectra, and (**f**) band edge positions versus the reduction potential of NHE of $g\text{-}C_3N_4$ and $LaFeO_3$ photocatalysts.

As shown in Figure 1b, the UV-visible absorption spectra of the as-synthesized $LaFeO_3$, $g\text{-}C_3N_4$, and $LaFeO_3/g\text{-}C_3N_4$ photocatalysts were measured using a UV-visible absorption spectrometer. A characteristic absorption edge is seen at 458 nm for pure $g\text{-}C_3N_4$, which is in line with the previously reported optical energy band gap value of 2.7 eV. $LaFeO_3$ has an absorption edge at 685 nm, which means it absorbs light in the visible spectrum (E_g = 1.81 eV). In perovskite-type oxide materials, the transition of electrons between the valence band (O 2p) and the conduction band (Fe 3d) is principally responsible for the strong absorption edges [34,35]. The absorption characteristic peak of $LaFeO_3/g\text{-}C_3N_4$ revealed extended visible light absorption, demonstrating that the synergistic interaction of the nanomaterials can alter the optical features of the base materials. From Tauc's plots shown in Figure 1c, we may infer the photocatalysts' band gaps. The predicted values for the energy band gaps (E_g) of the $g\text{-}C_3N_4$ and $LaFeO_3$ catalysts are 2.7 and 1.81 eV, respectively. After being exposed to visible light, semiconductors typically generate electron–hole pairs in the valence band and then the excited electrons are transferred to their conduction band. As shown in Figure 1d,e, we have explored the valence band XPS spectra of bare $g\text{-}C_3N_4$ and $LaFeO_3$ photocatalysts to gain insight into their precise valence and conduction bands. The predicted valence band potential values of pristine $g\text{-}C_3N_4$ and $LaFeO_3$ photocatalysts are 1.4 and 2.38 V, respectively. The conduction band potential

values of the catalysts were calculated according to the equation mentioned in our previous report [36]. Thus, the predicted conduction band potential values of pristine g-C_3N_4 and $LaFeO_3$ are −1.3 and 0.57 V vs. the NHE, respectively. Figure 1f demonstrates the energy band gaps and band edge potentials of g-C_3N_4 and $LaFeO_3$ photocatalysts.

To verify the microstructure of g-C_3N_4 and $LaFeO_3$/g-C_3N_4 catalysts, TEM and high-resolution TEM (HR-TEM) micrographs were recorded (Figure 2a–d). Figure 2a reveals the TEM micrograph of g-C_3N_4, which demonstrates that the material is composed of stacked layers of ultra-thin flat surface nanosheets with thicknesses of 80–100 nm. An HRTEM image displaying the distinctive structure of g-C_3N_4 is shown in Figure 2b. The aggregation of $LaFeO_3$ particles on the surface of g-C_3N_4 nanosheets could be obviously seen in the TEM micrograph of the $LaFeO_3$/g-C_3N_4 heterostructure (Figure 2c). The distinct lattice fringes of g-C_3N_4 and $LaFeO_3$ catalysts can be clearly seen in the HRTEM micrograph of the $LaFeO_3$/g-C_3N_4 catalyst (Figure 2d) [37]. This confirms the successful fabrication of $LaFeO_3$/g-C_3N_4 heterojunction.

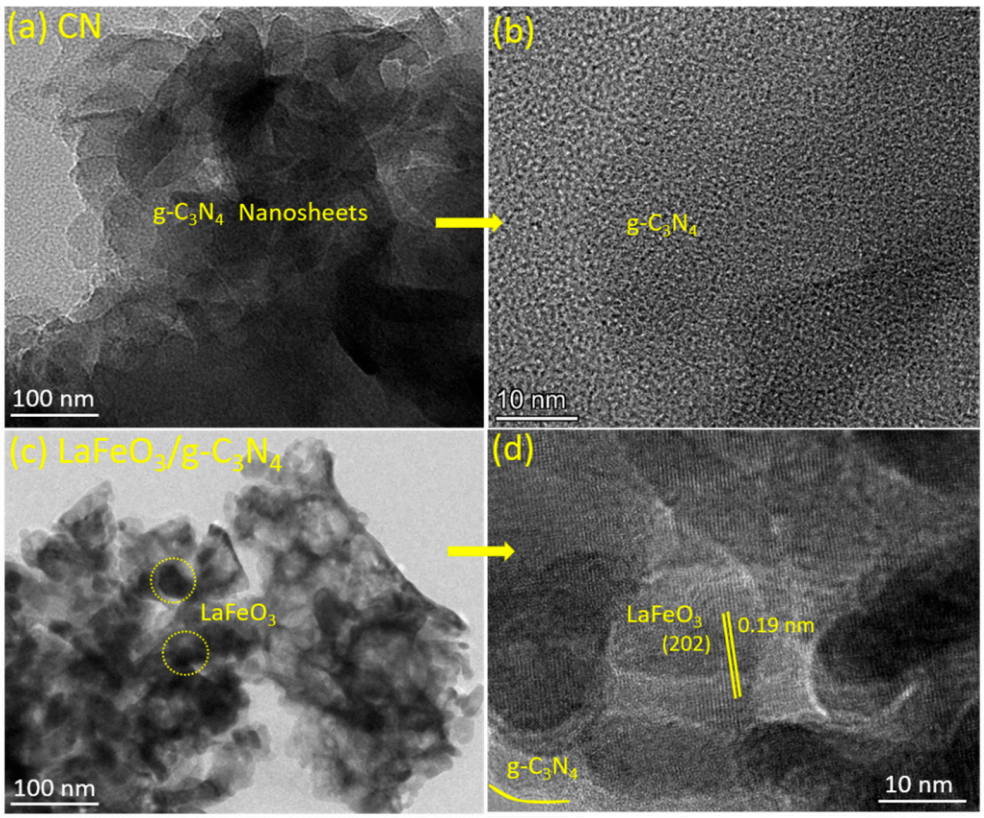

Figure 2. (**a**) TEM, and (**b**) HRTEM micrographs of g-C_3N_4 photocatalyst. (**c**) TEM and (**d**) HRTEM micrographs of $LaFeO_3$/g-C_3N_4 photocatalyst.

The elemental compositions of the g-C_3N_4 and $LaFeO_3$/g-C_3N_4 catalysts were studied by means of XPS analysis. The existence of relevant elements is revealed by the XPS survey spectra of the photocatalysts (Figure 3a). The deconvoluted C1s spectra (Figure 3b) demonstrate the existence of peaks at 284.75 and 288.15 eV, which are accredited to the Sp2 hybridized C atoms (i.e., N−C=N) and graphitic-carbon (i.e., C−N), respectively. Noticeably, after $LaFeO_3$ coupling, the binding energy peaks of g-C_3N_4 are somewhat shifted toward the higher binding energies side, possibly due to the charge transfer at the interface of the as-fabricated $LaFeO_3$/g-C_3N_4 heterojunction. The N 1s spectrum of bare g-C_3N_4 (Figure 3c) reveals two peaks at 398.6 and 401.2 eV, respectively, accredited to the Sp2-hybridized N atoms (i.e., C-N=C) by heptazine rings and the tertiary N atoms (i.e., N-$(C)_3$). The electron delocalization effect causes a comparable shift in the N 1s peak of the $LaFeO_3$/g-C_3N_4 catalyst [38].

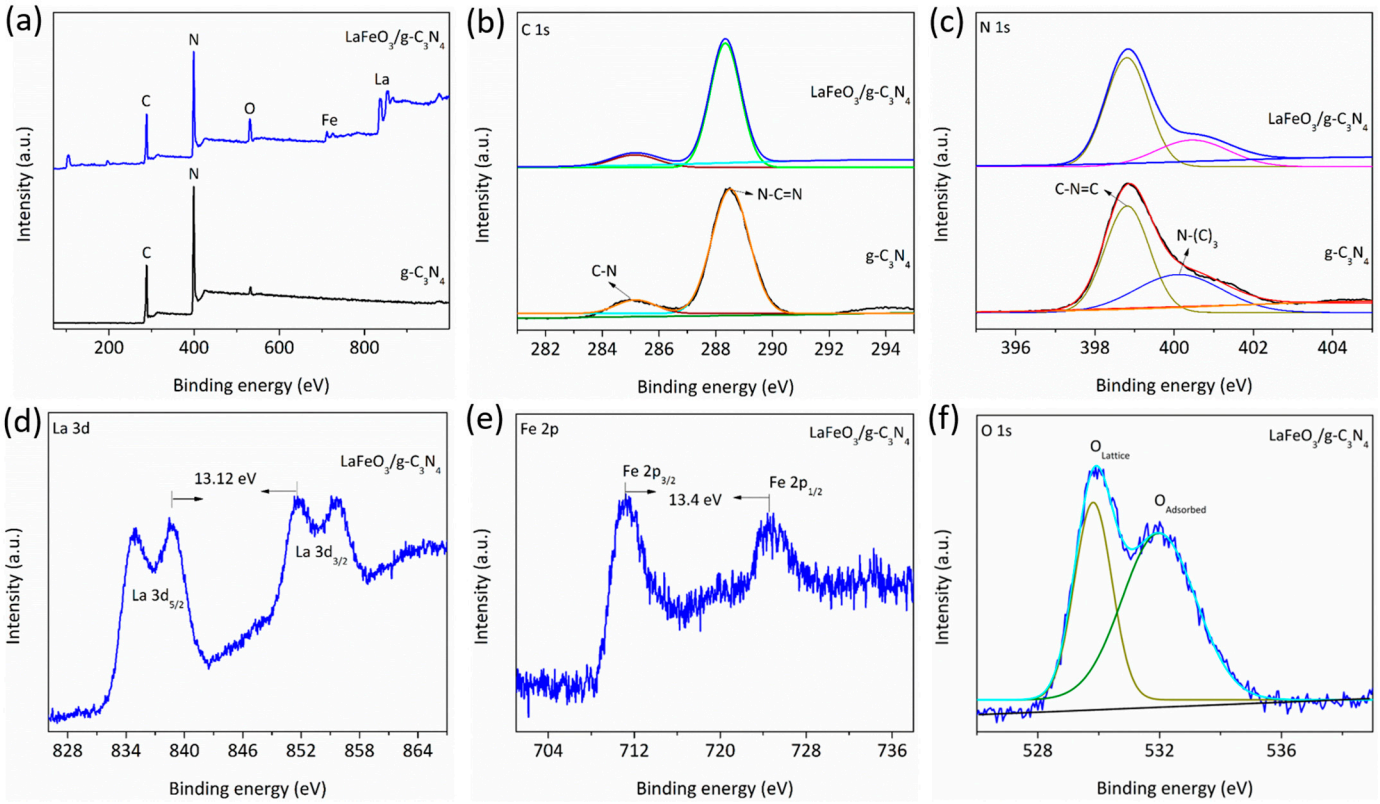

Figure 3. (**a**) XPS survey spectra, (**b**) deconvoluted high resolution C 1s spectra, and (**c**) deconvoluted high resolution N 1s spectra of g-C_3N_4 and $LaFeO_3$/g-C_3N_4 photocatalysts. (**d**) High-resolution La 3d spectrum, (**e**) high-resolution Fe 2p spectrum, and (**f**) deconvoluted high-resolution O 1s spectrum of $LaFeO_3$/g-C_3N_4 photocatalyst.

In addition, two distinct peaks can be seen in the La 3d XPS spectrum of the $LaFeO_3$/g-C_3N_4 catalyst (Figure 3d) at 834.65 and 851.55 eV. In addition, two small peaks originated at 838.6 and 855.2 eV corresponding to the satellite peaks of the La $3d_{5/2}$ and La $3d_{3/2}$ orbitals. These peaks are produced by the transferring of an electron from a 2p to an empty 4f orbital in the O_2 ligands. The spin-orbital splitting of the La $3d_{5/2}$ and La $3d_{3/2}$ orbitals is 16.6 eV, demonstrating the +3-oxidation state of La. The peaks originating at 710.1 (i.e., $2p_{3/2}$) and 723.65 eV (i.e., $2p_{1/2}$) in the Fe 2p spectrum of the $LaFeO_3$/g-C_3N_4 composite (Figure 3e) indicate the +3-oxidation state of the Fe in the composite. Lattice oxygen (i.e., La-O) and surface-adsorbed hydroxyl groups ($^{\bullet}$OH) are responsible for the two typical peaks at 530.15 and 532.55 eV in the deconvoluted O 1s XPS spectra of the $LaFeO_3$/g-C_3N_4 catalyst (Figure 3f) [27,39]. The XPS analysis shows that $LaFeO_3$ and g-C_3N_4 have strong interactions with each other.

2.2. Photogenerated Charge Separation

Photoluminescence (PL) spectroscopy was utilized to explore the photo-physics of photogenerated charges in the g-C_3N_4 and $LaFeO_3$/g-C_3N_4. The PL method can provide us with useful information about the presence of surface defects, vacancies, as well as charge recombination at the catalyst surface [40,41]. As is evident from Figure 4a, the g-C_3N_4 photocatalyst has a robust PL signal, which favors efficient recombination of charge carriers. However, the PL peak intensity is significantly suppressed for the $LaFeO_3$/g-C_3N_4 catalyst. Based on these findings, we may conclude that the $LaFeO_3$/g-C_3N_4 composite exhibits much lower charge recombination compared to that of the pristine g-C_3N_4. In addition, surface photo-voltage (SPV) spectroscopy indicates enhanced charge transfer and separation in the $LaFeO_3$/g-C_3N_4 catalyst. In semiconductors, SPV spectroscopy is typically employed to learn more about electron–hole pairs' excitation, separation, as well

as transfer at the surface. SPV typically detects a signal representing the charge separation. Increased charge carrier separation results in a robust SPV signal [42]. Figure 4b shows that the SPV signal from g-C_3N_4 is quite low. The $LaFeO_3$/g-C_3N_4 composite, on the other hand, shows a significantly higher SPV signal, indicating better charge separation and transfer in the fabricated heterojunction. Electrochemical impedance spectra (EIS) measurement is employed to confirm the findings of PL and SPV. In most cases, the arc radius of the resulting EIS Nyquist plots might be used to assess the charge transfer resistance of the catalysts. The huge arc radius is indicative of weak charge separation in semiconducting nanomaterials, as has been widely stated [43]. Figure 4c shows that the $LaFeO_3$/g-C_3N_4 catalyst has highly effective charge transfer and separation in comparison to that of the bare g-C_3N_4 catalyst, as proven by the short arc radius of the EIS Nyquist plot. The equivalent circuit model is provided as the inset of Figure 4c.

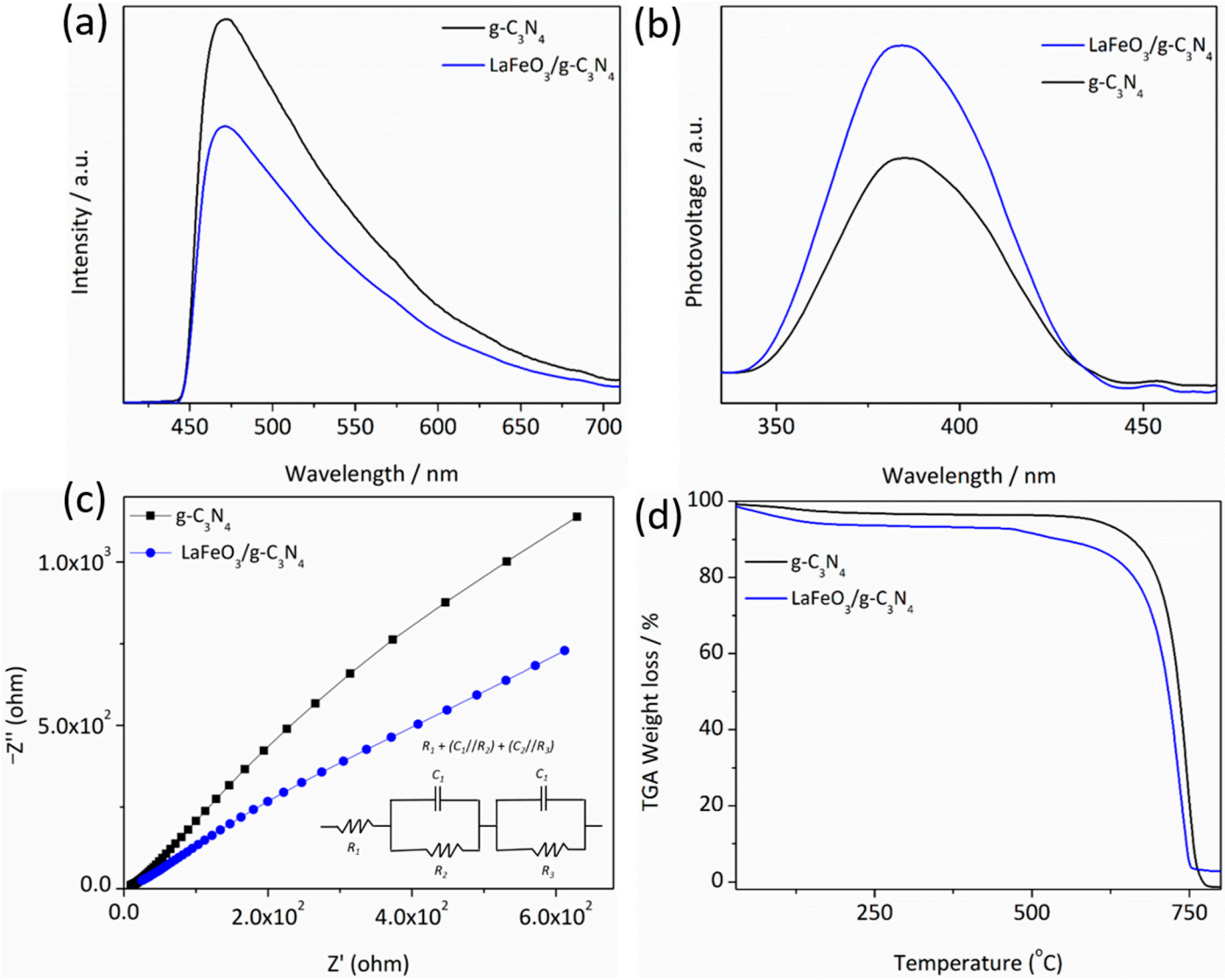

Figure 4. (**a**) PL spectra; (**b**) SPV spectra; (**c**) EIS Nyquist plots with inset the equivalent circuit model in which R_1 is the FTO glass resistance, C_1/R_2 is the impedance of the composite/electrolyte interface, and C_2/R_3 is the impedance of counter electrode/electrolyte interface; (**d**) TGA spectra of g-C_3N_4 and $LaFeO_3$/g-C_3N_4 photocatalysts.

2.3. Thermogravimetric Analysis

Figure 4d displays the thermogravimetric analysis (TGA) spectra for g-C_3N_4 and $LaFeO_3$/g-C_3N_4 catalysts. It is worth noting that between 750 and 770 °C, pure g-C_3N_4 loses a substantial amount of weight, likely due to disintegration or combustion. However, between 700 and 750 °C, the $LaFeO_3$/g-C_3N_4 composite shows a dramatic loss of weight. Like other g-C_3N_4-based photocatalysts, the lower weight is due to the coupling of $LaFeO_3$, which reduces the thermal stability of pure g-C_3N_4. After heating the photocatalyst to temperatures above 700 °C, the g-C_3N_4 percentage composition in the $LaFeO_3$/g-C_3N_4 catalyst is estimated to be around 92%.

2.4. Photocatalytic Activities

The visible light catalytic activity of g-C_3N_4 and $LaFeO_3$/g-C_3N_4 catalysts for hydrogen generation was investigated. The photocatalyst's performance for H_2 production was evaluated at 1 h intervals throughout the 4 h photocatalytic experiment. Upon exposure to visible light irradiations ($\lambda > 420$ nm), pristine g-C_3N_4 produced a tiny amount of H_2 (i.e., 24.0 μmol h^{-1} g^{-1}) with the assistance of co-catalyst Pt, as shown in Figure 5a. It is vital to highlight that the $LaFeO_3$ did not produce H_2 because of its unsuitable conduction band potential (i.e., 0.47 V) for water reduction. The amount of H_2 produced over the composite of $LaFeO_3$/g-C_3N_4 is 351 μmol h^{-1} g^{-1}, remarkably higher in comparison to that of the pristine g-C_3N_4 component. The enhanced separation and transfer of electron–hole pairs via the Z-scheme transfer system led to the exceptional activity of the $LaFeO_3$/g-C_3N_4 catalyst. A stability test of the $LaFeO_3$/g-C_3N_4 catalyst for H_2 evolution under visible light irradiation was conducted. Recyclability testing (Figure 5b) shows that after four consecutive photocatalytic re-cycles, the photocatalyst activity did not decline significantly. These findings identify the superior recycling performance and stability of $LaFeO_3$/g-C_3N_4 photocatalyst.

To validate the H_2 evolution results, the photocatalytic performance of the catalysts for the degradation of RhB and MB dyes was evaluated under visible-light irradiation for 2 h. Figure 5c shows that the RhB degradation over pristine g-C_3N_4 and $LaFeO_3$ photocatalysts is approximately 33 and 44%, respectively. Interestingly, the RhB degradation over the $LaFeO_3$/g-C_3N_4 photocatalyst is much more significant (i.e., 94%). Similarly, the pure g-C_3N_4 and $LaFeO_3$ photocatalysts degraded by about 27 and 39% of the MB, respectively. After 2 h of visible light irradiation, the $LaFeO_3$/g-C_3N_4 catalyst decomposed 87% of MB (Figure 5d). Meanwhile, the photocatalytic recyclability tests for the degradation of RhB and MB dyes were measured in order to confirm the stability of the $LaFeO_3$/g-C_3N_4 catalyst. As is obvious from Figure 5e,f, after 8 h of catalytic cycles (each lasting 2 h), the composite catalyst does not show any apparent decrease in catalytic performance for the degradation of RhB and MB dyes. Based on the above experiments, it is confirmed that coupling $LaFeO_3$ with g-C_3N_4 can greatly increase its surface redox ability due to the improved photogenerated charge separation in a Z-scheme direction.

In order to confirm which reactive intermediate species are involved in the degradation of RhB and MB dyes over the as-prepared $LaFeO_3$/g-C_3N_4 photocatalyst, radical trapping experiments were carried out to quench the reactive species such as holes (h^+), hydroxyl radicals ($^\bullet OH$), and superoxide radicals ($O_2^{\bullet -}$). Scavenging species such as ethylenediaminetetraacetic acid disodium salt (EDTA-2Na), isopropyl alcohol (IPA), and p-Benzoquinone (BQ) were employed to assess the contributions of h^+, $^\bullet OH$, and $O_2^{\bullet -}$ to the oxidation of RhB and MB dyes [40]. As revealed in Figure 6a,b, after 2 h of irradiation in the absence of any scavenger, approximately 94 and 87% of RhB and MB dyes were degraded over the $LaFeO_3$/g-C_3N_4 photocatalyst, respectively. However, after the addition of scavenger solutions (1 mmol) into the suspension containing RhB and MB dyes, only the IPA and BQ scavengers significantly reduced the degradation of both dyes. This suggests that the $^\bullet OH$, and $O_2^{\bullet -}$ radicals contributed considerably to the total degradation of RhB and MB dyes, while the role of h^+ was less significant. EPR spectroscopic investigation of the $^\bullet O_2$ and $^\bullet OH$ production during photocatalysis was carried out under dark and

light (10 min) conditions at room temperature, as shown in Figure 6c,d, respectively. The trapping reagents DMPO-•OH and DMPO-•O_2 were added to the solution containing the $LaFeO_3$/g-C_3N_4 photocatalyst under continuous stirring prior to EPR analysis. As expected, no peaks of DMPO-•OH and DMPO-•O_2 can be seen in the dark. Surprisingly, distinct peaks of DMPO-•OH and DMPO-•O_2 were identified following a 10 min visible light catalytic reaction. The significant redox power of the $LaFeO_3$/g-C_3N_4 photocatalyst is clarified, and the Z-scheme charge transfer mechanism is confirmed.

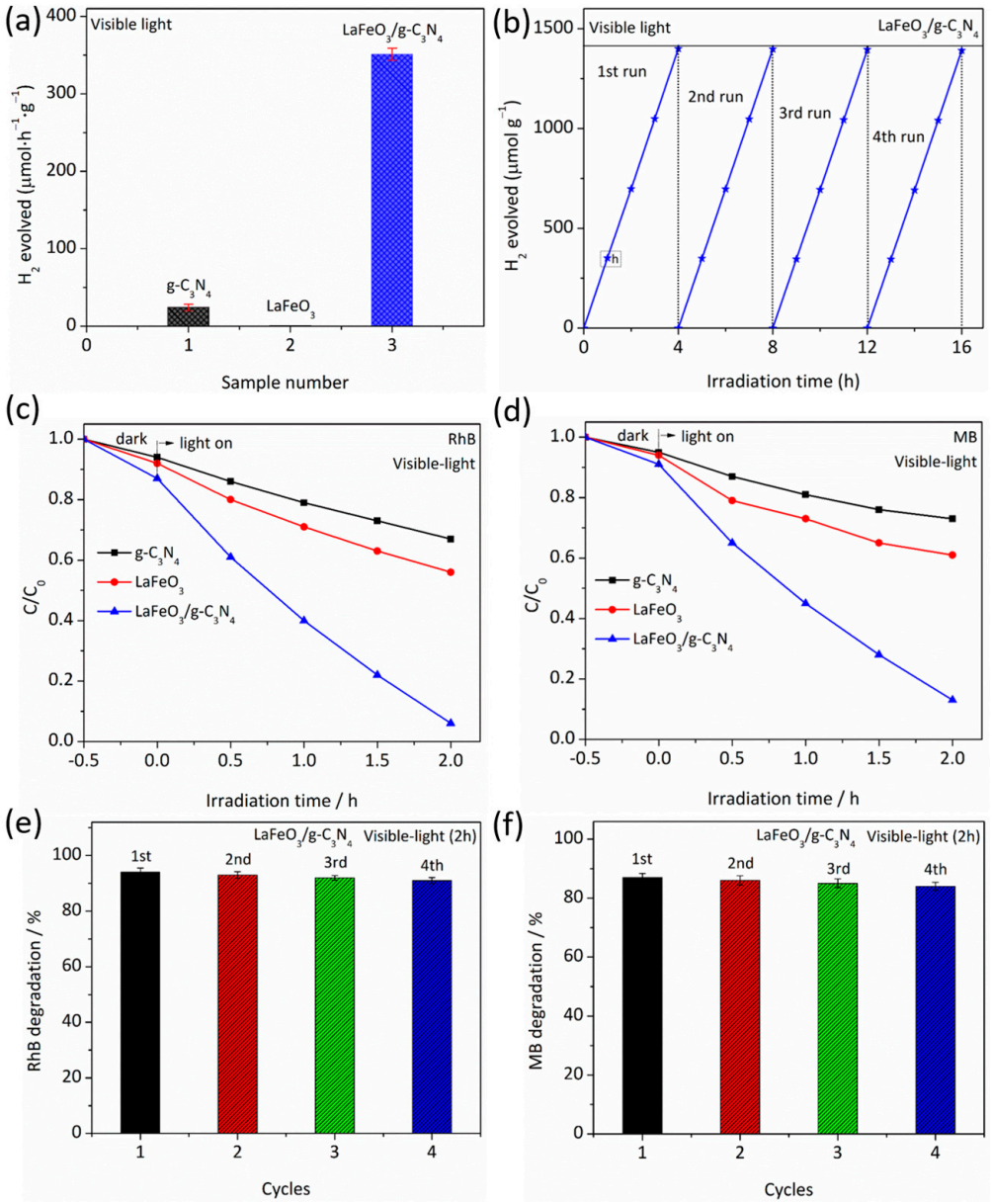

Figure 5. (**a**) Photocatalytic H_2 evolution over g-C_3N_4, $LaFeO_3$, and $LaFeO_3$/g-C_3N_4 photocatalysts. (**b**) Stability test for H_2 evolution $LaFeO_3$/g-C_3N_4 photocatalyst. (**c**) Photocatalytic degradation of RhB and (**d**) photocatalytic degradation of MB over the g-C_3N_4, $LaFeO_3$, and $LaFeO_3$/g-C_3N_4 photocatalysts. (**e**) Photocatalytic recyclability test for RhB degradation and (**f**) photocatalytic recyclability test for MB degradation over $LaFeO_3$/g-C_3N_4 photocatalyst.

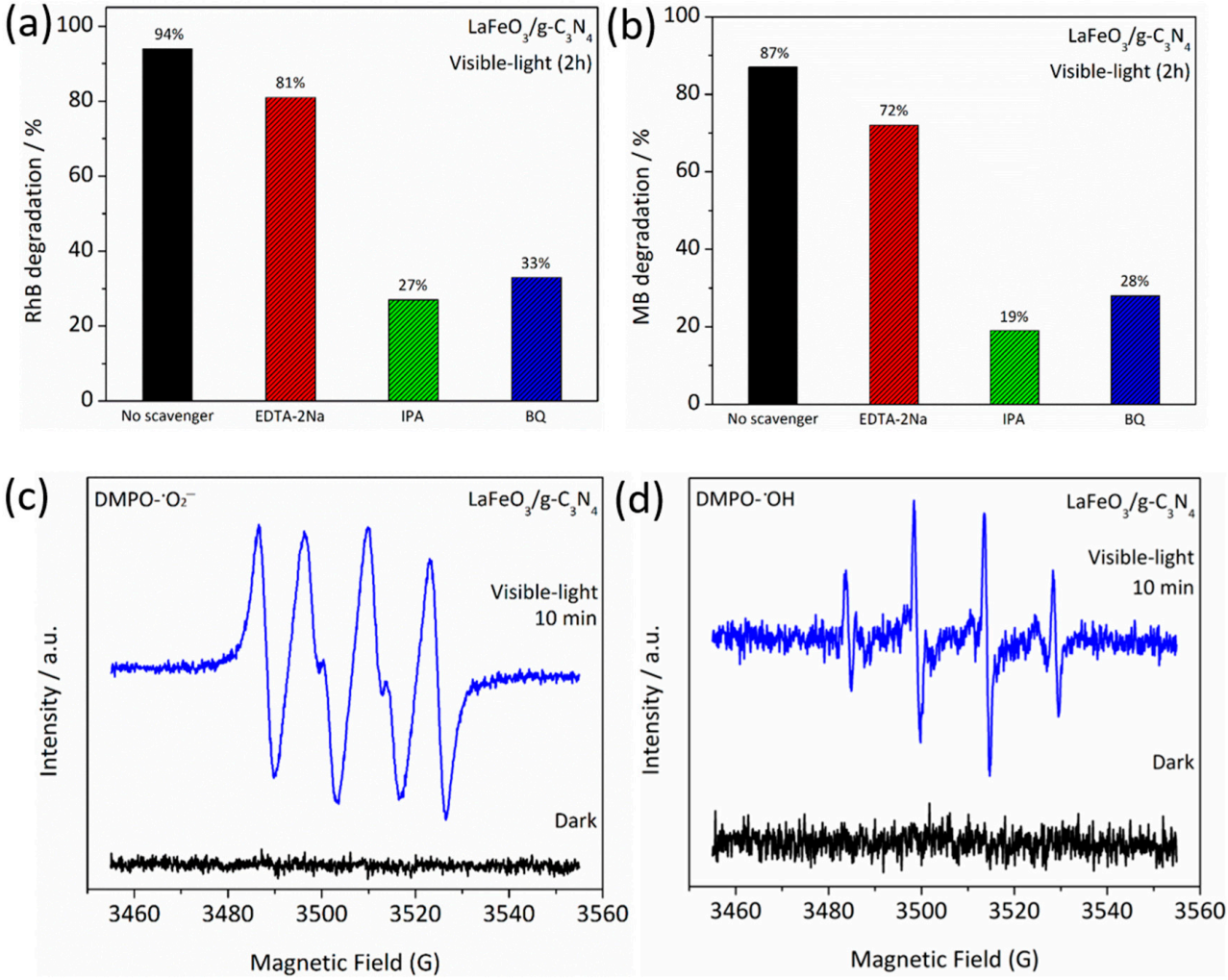

Figure 6. (**a**) Scavenging experiments for RhB degradation and (**b**) scavenging experiments for MB degradation. (**c**) EPR spectra of $^{\bullet}O_2^-$ and (**d**) EPR spectra of $^{\bullet}OH$ for $LaFeO_3/g\text{-}C_3N_4$ photocatalyst.

2.5. Mechanism

Based on the obtained results, a schematic for charge carrier generation, separation, transfer, and photocatalytic activities over the $LaFeO_3/g\text{-}C_3N_4$ Z-scheme system is depicted in Figure 7. The predicted band gap values of $LaFeO_3$ and $g\text{-}C_3N_4$ catalysts are 1.81 and 2.7 eV, respectively. Notably, the valence band potentials of $g\text{-}C_3N_4$ and $LaFeO_3$ photocatalysts are 1.4 and 2.38 V, respectively. In addition, the conduction band potentials of $g\text{-}C_3N_4$ and $LaFeO_3$ photocatalysts are calculated to be −1.3 and 0.57 V, respectively. When $LaFeO_3$ is coupled with $g\text{-}C_3N_4$, a heterojunction of $LaFeO_3/g\text{-}C_3N_4$ is formed. Charge carriers (electron–hole pairs) are generated in both components of the $LaFeO_3/g\text{-}C_3N_4$ heterojunction when exposed to visible light. Consequently, the electrons in both components are stimulated to their respective conduction bands. Meanwhile, holes continue to appear in their corresponding valence bands. The recombination between electrons of $LaFeO_3$ and holes of $g\text{-}C_3N_4$ occurs due to the proximity of the conduction band of $LaFeO_3$ and the valence band of $g\text{-}C_3N_4$. Thus, the transfer of charges occurs in a Z-scheme direction in the as-fabricated $LaFeO_3/g\text{-}C_3N_4$ catalyst. This improves charge carriers' separation in the as-fabricated $LaFeO_3/g\text{-}C_3N_4$ catalyst. It is important to note that the standard potentials for water reduction and superoxide radical ($^{\bullet}O_2^-$) generation are 0 and −0.046 V, respectively, versus the reduction potential of a Normal Hydrogen Electrode (NHE) [44]. The standard potential for hydroxyl radical ($^{\bullet}OH$) production is 2.27 V vs. the NHE [45]. Consequently, photogenerated electrons in the $g\text{-}C_3N_4$ conduction band reduce water to H_2 and O_2 to $^{\bullet}O_2^-$. Moreover, the valence band holes of $LaFeO_3$ will react with water and

surface-adsorbed hydroxyl groups to produce $^{\bullet}OH$. The EPR study confirms the existence of both the $^{\bullet}OH$ and $^{\bullet}O_2$ radicals. Therefore, the RhB and MB dyes are oxidized by a combination of $^{\bullet}OH$ and $^{\bullet}O_2$. Furthermore, the photogeneration could also contribute to the total degradation of organic dyes. The above results reveal that the charge separation in the fabricated $LaFeO_3/g\text{-}C_3N_4$ Z-scheme heterojunction is significantly promoted which led to improved H_2 evolution and dyes degradation performance. According to the charge transfer phenomenon in the $LaFeO_3/g\text{-}C_3N_4$ Z-scheme photocatalyst, the catalytic reactions would proceed in a fashion as mentioned in Equations (1)–(7):

$$LaFeO_3/g\text{-}C_3N_4 + h\nu \rightarrow LaFeO_3\ (e^- + h^+)/g\text{-}C_3N_4\ (e^- + h^+) \quad (1)$$

$$g\text{-}C_3N_4\ (e^-) + 2H^+ \rightarrow H_2 \quad (2)$$

$$g\text{-}C_3N_4\ (e^-) + O_2 \rightarrow {}^{\bullet}O_2{}^- \quad (3)$$

$$LaFeO_3\ (h^+) + OH^-/H_2O \rightarrow {}^{\bullet}OH \quad (4)$$

$$LaFeO_3\ (h^+) + \text{Dyes} \rightarrow \text{Degradation Products} \quad (5)$$

$${}^{\bullet}O_2{}^- + \text{Dyes} \rightarrow \text{Degradation Products} \quad (6)$$

$${}^{\bullet}OH + \text{Dyes} \rightarrow \text{Degradation Products} \quad (7)$$

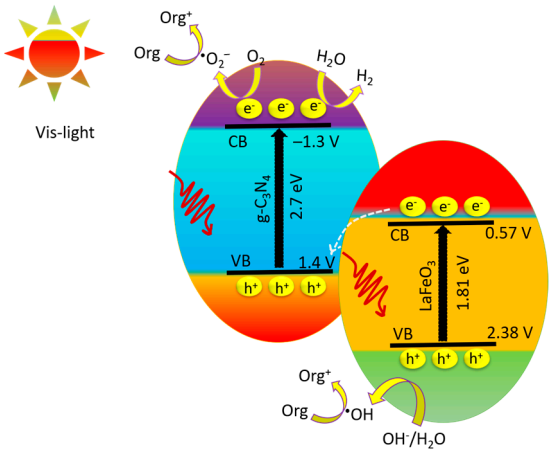

Figure 7. The energy band gaps, valence band, conduction band potentials, charge carriers' separation and transfer, and surface redox reactions over the Z-scheme $LaFeO_3/g\text{-}C_3N_4$ photocatalyst.

3. Materials and Methods

Analytical-grade solvents/reagents were used in this study without being further purified.

3.1. Fabrication of g-C_3N_4

An amount of 5 g of melamine was directly calcined in an air environment at 550 °C (5 °C min^{-1}) for 2 h in a furnace. After reaching room temperature, the product was collected and milled into a fine powder.

3.2. Fabrication of $LaFeO_3$ Nanoparticles

A sol–gel process was used to fabricate $LaFeO_3$ nanoparticles. In a typical procedure, an equimolar (0.1 M) precursor solution of $La(NO_3)_3{\cdot}6H_2O$ and $Fe(NO_3)_3{\cdot}9H_2O$ was prepared in methanol/ethylene glycol (1:1) mixture and stirred under room temperature for half an hour. After that, both solutions were mixed under continuous stirring and then kept under ultrasonic treatment for half an hour. The mixed solution was then stirred for 16 h and then dried at 85 °C. Consequently, the dried powder was calcined in air at 650 °C for 2 h to obtain $LaFeO_3$ nanoparticles.

3.3. Fabrication of $LaFeO_3$/g-C_3N_4 Composite

A wet chemical approach was used to fabricate the $LaFeO_3$/g-C_3N_4 heterostructure composite. A 5wt% of $LaFeO_3$ to that of the corresponding g-C_3N_4 (total weight of the sample was 1 g) was dispersed in a beaker containing 25 mL of water/ethanol mixture (1:1) and continuously stirred for 12 h. Then, the powder dispersed in the solvent mixture was centrifuged and washed with de-ionized water and ethanol. Finally, it was dried in an oven at 85 °C, milled into a fine powder, and then calcined at 450 °C (5 °C min^{-1}) for 2 h.

3.4. Characterization

A Bruker-D8 powder diffractometer (Chiba, Japan) was employed to acquire the X-ray diffraction patterns of the catalysts using a CuKα radiation source. A UV-2550 Shimadzu-Kyoto, Japan Spectrophotometer was used to obtain the UV-vis absorption spectra. The TEM images were taken via a transmission electron microscope (TEM) model (JEOL Ltd-JEM-2100, Tokyo, Japan) set at 200 kV. An Ultra-DLD-Kratos-Axis X-ray photoelectron spectroscope (XPS) (Kyoto, Japan) with Al (mono) X-ray source was employed to detect the chemical composition and elemental states of the catalysts. An FP-6500 (Tokyo, Japan) fluorescence spectrometer was utilized to detect the PL spectra of the catalysts. Surface photovoltage (SPV) spectra were measured using equipment linked with a lock-in amplifier (model SR830, Sunnyvale, CA, USA) and a light chopper (model SR540, Sunnyvale, CA, USA). A Perkin Elmer TGA-8000 (USA) was used for a thermogravimetric study in the temperature range of 30–780 °C under air conditions. Electrochemical impedance spectroscopy (EIS) spectra were obtained with Shanghai Chenhua CHI-760E equipment (Shanghai, China) while employing a Ag/AgCl reference electrode. For electron paramagnetic resonance (EPR) spectra measurement, a Bruker-A300 (Beijing, China) apparatus was used. The EPR measurement was performed at room temperature, and the trapping reagent 5,5-Dimethyl-1-pyrroline-N-oxide (DMPO) was utilized.

3.5. Photocatalytic Experiments

The photocatalytic H_2 production experiments were carried out in a sealed 250 mL quartz reactor. During the test, methanol was added as a sacrificial agent. About 50 mg of the photocatalyst powder was diffused in a mixture of water (80 mL)/methanol (20 mL) under continuous stirring. To remove bubbles, the system was extensively evacuated for half an hour. The system was then irradiated under a Perfect-light 300 W Xenon lamp (Beijing Perfect light Technology Co., Ltd) with a cut-off filter ($\lambda > 420$ nm). The hydrogen produced during the photocatalytic reaction was measured at a fixed time interval (1 h) and detected via an online gas chromatograph (CEAULIGH, GC-7920 with carrier gas N_2) linked to a TCD detector. The photocatalytic recyclability test for H_2 production over the $LaFeO_3$/g-C_3N_4 photocatalyst was evaluated for 16 h (4 cycles, each lasting 4 h) under the same experimental conditions. The photocatalytic experiments for Rhodamine B (RhB) and Methylene Blue (MB) were performed in a 100 mL volume quartz reactor with the assistance of a 300 W Xe lamp (cut-off filter $\lambda > 420$ nm). The duration of each experiment was 2 h. Before photocatalytic reaction, the dye solutions containing catalysts (50 mg) were stirred in the dark for 30 min to attain adsorption equilibrium. Similarly, the photocatalytic recyclable tests for the dyes' degradation over the $LaFeO_3$/g-C_3N_4 photocatalyst were evaluated for 8 h (4 cycles, each lasting 2 h) under the same experimental conditions. The scavenger-

trapping experiments were performed under the same experimental conditions with the assistance of ethylenediaminetetraacetic acid disodium salt (EDTA-2Na), isopropyl alcohol (IPA), and p-Benzoquinone (BQ) as the h^+, $^{\bullet}OH$, and $O_2^{\bullet-}$ trapping agents, respectively.

4. Conclusions

In summary, the fabrication of the Z-scheme $LaFeO_3/g\text{-}C_3N_4$ system for water reduction to evolve hydrogen and organic dye degradation is described in this study. Notably, the as-fabricated $LaFeO_3/g\text{-}C_3N_4$ composite catalyst revealed outstanding water reduction performance to generate H_2 (i.e., 351 mol $h^{-1}g^{-1}$) under visible light irradiation, which is significantly higher in comparison to that of the $g\text{-}C_3N_4$. Additionally, the photocatalyst oxidized 87% of the MB dye and 94% of the RhB dye after two hours of visible light irradiation. The results indicate that the significantly increased photo-activities of the $LaFeO_3/g\text{-}C_3N_4$ Z-scheme heterostructure are due to extended light absorption and dramatically accelerated charge carrier separation. The development of this highly efficient Z-scheme heterostructure photocatalyst offers a promising strategy for the design and implementation of efficient Z-scheme systems to address energy and environmental concerns.

Author Contributions: Conceptualization, M.H. and M.B.; methodology, A.K.; validation, M.H. and M.B.; formal analysis, M.H. and A.B.; investigation, M.H.; resources, M.B.; data curation, M.H.; writing—original draft preparation, M.H. and A.K.; writing—review and editing, M.B.; supervision, M.B.; project administration, M.H.; funding acquisition, M.H. and M.B. All authors have read and agreed to the published version of the manuscript.

Funding: This research received no external funding.

Data Availability Statement: Data will be available from the corresponding author upon reasonable request.

Acknowledgments: Authors thank Prince Sultan University for the financial support.

Conflicts of Interest: The authors declare no conflict of interest.

Sample Availability: Samples of the compounds are not available from the authors.

References

1. Fang, M.; Tan, X.; Liu, Z.; Hu, B.; Wang, X. Recent Progress on Metal-Enhanced Photocatalysis: A Review on the Mechanism. *Research* **2021**, *2021*, 9794329. [CrossRef] [PubMed]
2. Hu, J.; Guo, X.W.; Zhang, Y.C.; Zhang, F. Review on the Advancement of SnS_2 in the Photocatalysis. *J. Mater. Chem. A* **2023**, *11*, 7331–7343.
3. Nnabuife, S.G.; Ugbeh-Johnson, J.; Okeke, N.E.; Ogbonnaya, C. Present and Projected Developments in Hydrogen Production: A Technological Review. *Carbon Capture Sci. Technol.* **2022**, *3*, 100042. [CrossRef]
4. Qazi, A.; Hussain, F.; Rahim, N.A.; Hardaker, G.; Alghazzawi, D.; Shaban, K.; Haruna, K. Towards Sustainable Energy: A Systematic Review of Renewable Energy Sources, Technologies, and Public Opinions. *IEEE Access* **2019**, *7*, 63837–63851. [CrossRef]
5. Pan, X.; Shao, T.; Zheng, X.; Zhang, Y.; Ma, X.; Zhang, Q. Energy and Sustainable Development Nexus: A Review. *Energy Strategy Rev.* **2023**, *47*, 101078. [CrossRef]
6. Kabeyi, M.J.B.; Olanrewaju, O.A. Sustainable Energy Transition for Renewable and Low Carbon Grid Electricity Generation and Supply. *Front. Energy Res.* **2022**, *9*, 743114. [CrossRef]
7. Noureen, L.; Wang, Q.; Humayun, M.; Shah, W.A.; Xu, Q.; Wang, X. Recent Advances in Structural Engineering of Photocatalysts for Environmental Remediation. *Environ. Res.* **2023**, *219*, 115084. [CrossRef]
8. Khan, N.A.; Humayun, M.; Usman, M.; Ghazi, Z.A.; Naeem, A.; Khan, A.; Khan, A.L.; Tahir, A.A.; Ullah, H. Structural Characteristics and Environmental Applications of Covalent Organic Frameworks. *Energies* **2021**, *14*, 2267. [CrossRef]
9. Li, J.; Yuan, H.; Zhang, W.; Jin, B.; Feng, Q.; Huang, J.; Jiao, Z. Advances in Z-scheme Semiconductor Photocatalysts for the Photoelectrochemical Applications: A Review. *Carbon Energy* **2022**, *4*, 294–331. [CrossRef]
10. Wang, H.; Zhang, L.; Chen, Z.; Hu, J.; Li, S.; Wang, Z.; Liu, J.; Wang, X. Semiconductor Heterojunction Photocatalysts: Design, Construction, and Photocatalytic Performances. *Chem. Soc. Rev.* **2014**, *43*, 5234–5244. [CrossRef]
11. Liu, Z.; Yu, Y.; Zhu, X.; Fang, J.; Xu, W.; Hu, X.; Li, R.; Yao, L.; Qin, J.; Fang, Z. Semiconductor Heterojunctions for Photocatalytic Hydrogen Production and Cr(VI) Reduction: A review. *Mater. Res. Bull.* **2022**, *147*, 111636. [CrossRef]
12. Low, J.; Yu, J.; Jaroniec, M.; Wageh, S.; Al-Ghamdi, A.A. Heterojunction Photocatalysts. *Adv. Mater.* **2017**, *29*, 1601694. [CrossRef] [PubMed]

13. Tahir, M.; Tasleem, S.; Tahir, B. Recent Development in Band Engineering of Binary Semiconductor Materials for Solar Driven Photocatalytic Hydrogen Production. *Int. J. Hydrog. Energy* **2020**, *45*, 15985–16038. [CrossRef]
14. Cao, S.; Yu, J. g-C_3N_4-Based Photocatalysts for Hydrogen Generation. *J. Phys. Chem. Lett.* **2014**, *5*, 2101–2107. [CrossRef]
15. Alhebshi, A.; Sharaf Aldeen, E.; Mim, R.S.; Tahir, B.; Tahir, M. Recent Advances in Constructing Heterojunctions of Binary Semiconductor Photocatalysts for Visible Light Responsive CO_2 Reduction to Energy Efficient Fuels: A Review. *Int. J. Energy Res.* **2022**, *46*, 5523–5584. [CrossRef]
16. Lee, J.-T.; Lee, S.-W.; Wey, M.-Y. S-scheme g-C_3N_4/ZnO Heterojunction Photocatalyst with Enhanced Photodegradation of Azo Dye. *J. Taiwan Inst. Chem. Eng.* **2022**, *134*, 104357. [CrossRef]
17. Kadi, M.W.; El-Hout, S.I.; Shawky, A.; Mohamed, R.M. Enhanced Mercuric Ions Reduction over Mesoporous S-scheme $LaFeO_3$/ZnO p-n Heterojunction Photocatalysts. *J. Taiwan Inst. Chem. Eng.* **2022**, *138*, 104476. [CrossRef]
18. Irshad, M.; tul Ain, Q.; Zaman, M.; Aslam, M.Z.; Kousar, N.; Asim, M.; Rafique, M.; Siraj, K.; Tabish, A.N.; Usman, M. Photocatalysis and Perovskite Oxide-Based Materials: A Remedy for a Clean and Sustainable Future. *RSC Adv.* **2022**, *12*, 7009–7039. [CrossRef]
19. Huang, C.-W.; Hsu, S.-Y.; Lin, J.-H.; Jhou, Y.; Chen, W.-Y.; Lin, K.-Y.A.; Lin, Y.-T.; Nguyen, V.-H. Solar-Light-Driven $LaFe_xNi_{1-x}O_3$ Perovskite Oxides for Photocatalytic Fenton-like Reaction to Degrade Organic Pollutants. *Beilstein J. Nanotechnol.* **2022**, *13*, 882–895. [CrossRef]
20. Yaseen, M.; Humayun, M.; Khan, A.; Idrees, M.; Shah, N.; Bibi, S. Photo-Assisted Removal of Rhodamine B and Nile Blue Dyes from Water Using CuO-SiO_2 Composite. *Molecules* **2022**, *27*, 5343. [CrossRef]
21. Yaseen, M.; Khan, A.; Humayun, M.; Farooq, S.; Shah, N.; Bibi, S.; Khattak, Z.A.K.; Rehman, A.U.; Ahmad, S.; Ahmad, S.M.; et al. Facile Synthesis of $Fe_3O_4-SiO_2$ Nanocomposites for Wastewater Treatment. *Macromol. Mater. Eng.* **2023**, 2200695. [CrossRef]
22. Wen, J.; Xie, J.; Chen, X.; Li, X. A Review on g-C_3N_4-Based Photocatalysts. *Appl. Surf. Sci.* **2017**, *391*, 72–123. [CrossRef]
23. Liu, R.; Chen, Z.; Yao, Y.; Li, Y.; Cheema, W.A.; Wang, D.; Zhu, S. Recent Advancements in gC_3N_4-Based Photocatalysts for Photocatalytic CO_2 Reduction: A Mini Review. *RSC Adv.* **2020**, *10*, 29408–29418. [CrossRef] [PubMed]
24. Catherine, H.N.; Chiu, W.-L.; Chang, L.-L.; Tung, K.-L.; Hu, C. Gel-like Ag-Dicyandiamide Metal–Organic Supramolecular Network-Derived g-C_3N_4 for Photocatalytic Hydrogen Generation. *ACS Sustain. Chem. Eng.* **2022**, *10*, 8360–8369. [CrossRef]
25. Huang, H.; Jiang, L.; Yang, J.; Zhou, S.; Yuan, X.; Liang, J.; Wang, H.; Wang, H.; Bu, Y.; Li, H. Synthesis and Modification of Ultrathin g-C_3N_4 for Photocatalytic Energy and Environmental Applications. *Renew. Sustain. Energy Rev.* **2023**, *173*, 113110. [CrossRef]
26. Humayun, M.; Ullah, H.; Usman, M.; Habibi-Yangjeh, A.; Tahir, A.A.; Wang, C.; Luo, W. Perovskite-type Lanthanum Ferrite Based Photocatalysts: Preparation, Properties, and Applications. *J. Energy Chem.* **2022**, *66*, 314–338. [CrossRef]
27. Khan, I.; Luo, M.; Guo, L.; Khan, S.; Shah, S.A.; Khan, I.; Khan, A.; Wang, C.; Ai, B.; Zaman, S. Synthesis of Phosphate-Bridged g-C_3N_4/$LaFeO_3$ Nanosheets Z-scheme Nanocomposites as Efficient Visible Photocatalysts for CO_2 Reduction and Malachite Green Degradation. *Appl. Catal. A* **2022**, *629*, 118418. [CrossRef]
28. Hu, C.; Yu, B.; Zhu, Z.; Zheng, J.; Wang, W.; Liu, B. Construction of Novel S-scheme $LaFeO_3$/g-C_3N_4 Composite with Efficient Photocatalytic Capacity for Dye Degradation and Cr (VI) Reduction. *Colloids Surf. A Physicochem. Eng. Asp.* **2023**, *664*, 131189. [CrossRef]
29. Ismael, M.; Wu, Y. A Facile Synthesis Method for Fabrication of $LaFeO_3$/gC_3N_4 Nanocomposite as Efficient Visible-Light-Driven Photocatalyst for Photodegradation of RhB and 4-CP. *New J. Chem.* **2019**, *43*, 13783–13793. [CrossRef]
30. Raziq, F.; Hayat, A.; Humayun, M.; Mane, S.K.B.; Faheem, M.B.; Ali, A.; Zhao, Y.; Han, S.; Cai, C.; Li, W. Photocatalytic Solar Fuel Production and Environmental Remediation through Experimental and DFT Based Research on CdSe-QDs-coupled P-doped-g-C_3N_4 Composites. *Appl. Catal. B* **2020**, *270*, 118867. [CrossRef]
31. Raziq, F.; He, J.; Gan, J.; Humayun, M.; Faheem, M.B.; Iqbal, A.; Hayat, A.; Fazal, S.; Yi, J.; Zhao, Y. Promoting Visible-Light Photocatalytic Activities for Carbon Nitride Based 0D/2D/2D Hybrid System: Beyond the Conventional 4-electron Mechanism. *Appl. Catal. B* **2020**, *270*, 118870. [CrossRef]
32. Humayun, M.; Li, Z.; Sun, L.; Zhang, X.; Raziq, F.; Zada, A.; Qu, Y.; Jing, L. Coupling of Nanocrystalline Anatase TiO_2 to Porous Nanosized $LaFeO_3$ for Efficient Visible-Light Photocatalytic Degradation of Pollutants. *Nanomaterials* **2016**, *6*, 22. [CrossRef] [PubMed]
33. Aizat, A.; Aziz, F.; Mohd Sokri, M.N.; Sahimi, M.S.; Yahya, N.; Jaafar, J.; Wan Salleh, W.N.; Yusof, N.; Ismail, A.F. Photocatalytic Degradation of Phenol by $LaFeO_3$ Nanocrystalline Synthesized by Gel Combustion Method via Citric Acid Route. *SN Appl. Sci.* **2019**, *1*, 1–10. [CrossRef]
34. Zhu, J.; Li, H.; Zhong, L.; Xiao, P.; Xu, X.; Yang, X.; Zhao, Z.; Li, J. Perovskite Oxides: Preparation, Characterizations, and Applications in Heterogeneous Catalysis. *ACS Catal.* **2014**, *4*, 2917–2940. [CrossRef]
35. Badro, J.; Rueff, J.-P.; Vanko, G.; Monaco, G.; Fiquet, G.; Guyot, F. Electronic Transitions in Perovskite: Possible Nonconvecting Layers in the Lower Mantle. *Science* **2004**, *305*, 383–386. [CrossRef]
36. Neena, D.; Humayun, M.; Bhattacharyya, D.; Fu, D. Hierarchical Sr-ZnO/g-C_3N_4 Heterojunction with Enhanced Photocatalytic Activities. *J. Photochem. Photobiol. A* **2020**, *396*, 112515.
37. Xu, K.; Feng, J. Superior Photocatalytic Performance of $LaFeO_3$/gC_3N_4 Heterojunction Nanocomposites under Visible Light Irradiation. *RSC Adv.* **2017**, *7*, 45369–45376. [CrossRef]

38. Acharya, S.; Mansingh, S.; Parida, K. The Enhanced Photocatalytic Activity of gC_3N_4-$LaFeO_3$ for the Water Reduction Reaction through a Mediator free Z-scheme Mechanism. *Inorg. Chem. Front.* **2017**, *4*, 1022–1032. [CrossRef]
39. Zhang, J.; Zhu, Z.; Jiang, J.; Li, H. Fabrication of a Novel AgI/$LaFeO_3$/g-C_3N_4 dual Z-scheme Photocatalyst with Enhanced Photocatalytic Performance. *Mater. Lett.* **2020**, *262*, 127029. [CrossRef]
40. Humayun, M.; Sun, N.; Raziq, F.; Zhang, X.; Yan, R.; Li, Z.; Qu, Y.; Jing, L. Synthesis of ZnO/Bi-doped Porous $LaFeO_3$ Nanocomposites as Highly Efficient Nano-photocatalysts Dependent on the Enhanced Utilization of Visible-Light-Excited Electrons. *Appl. Catal. B* **2018**, *231*, 23–33. [CrossRef]
41. Humayun, M.; Zada, A.; Li, Z.; Xie, M.; Zhang, X.; Qu, Y.; Raziq, F.; Jing, L. Enhanced Visible-Light Activities of Porous $BiFeO_3$ by Coupling with Nanocrystalline TiO_2 and Mechanism. *Appl.Catal. B* **2016**, *180*, 219–226. [CrossRef]
42. Raziq, F.; Qu, Y.; Humayun, M.; Zada, A.; Yu, H.; Jing, L. Synthesis of SnO_2/BP Codoped g-C_3N_4 Nanocomposites as Efficient Cocatalyst-Free Visible-Light Photocatalysts for CO_2 Conversion and Pollutant Degradation. *Appl. Catal. B* **2017**, *201*, 486–494. [CrossRef]
43. Zhao, R.; Sun, X.; Jin, Y.; Han, J.; Wang, L.; Liu, F. Au/Pd/gC_3N_4 Nanocomposites for Photocatalytic Degradation of Tetracycline Hydrochloride. *J. Mater. Sci.* **2019**, *54*, 5445–5456. [CrossRef]
44. Usman, M.; Zeb, Z.; Ullah, H.; Suliman, M.H.; Humayun, M.; Ullah, L.; Shah, S.N.A.; Ahmed, U.; Saeed, M. A Review of Metal-Organic Frameworks/Graphitic Carbon Nitride Composites for Solar-Driven Green H_2 Production, CO_2 Reduction, and Water Purification. *J. Environ. Chem. Eng.* **2022**, *10*, 107548. [CrossRef]
45. Chen, D.; Cheng, Y.; Zhou, N.; Chen, P.; Wang, Y.; Li, K.; Huo, S.; Cheng, P.; Peng, P.; Zhang, R. Photocatalytic Degradation of Organic Pollutants using TiO_2-based Photocatalysts: A Review. *J. Clean. Prod.* **2020**, *268*, 121725. [CrossRef]